

UNSTEADY PARAMETRIZATION OF A MORPHING WING DESIGN FOR IMPROVED AERODYNAMIC PERFORMANCE

Chawki Abdessemed, Yufeng Yao*, Pritesh Narayan and Abdesslem Bouferrouk
Department of Engineering Design and Mathematics, University of the West of England, Coldharbour Lane,
Frenchay, Bristol BS16 1QY, United Kingdom
*Corresponding author: Yufeng.Yao@uwe.ac.uk

ABSTRACT

A morphing wing is a bio-inspired concept where all moving parts e.g. slats/flaps are replaced with a deformable body. This paper describes a methodology that uses modified parametrization methods to define a morphing geometry, and applies user-defined function (UDF) to generate dynamic meshing around it for unsteady flow analysis. To verify mesh quality during deformation, steady CFD results of a deformed mesh at a 'frozen' time-step were compared to those from a re-generated mesh over a range of angles of attack. It was found that results from a deformed and re-generated mesh are in good agreement, confirming the validity of dynamic meshing. Furthermore, a comparison study between a morphed and flapped airfoil was performed, where it was observed that the morphed airfoil produced higher lift/drag ratio than the flapped one. Finally, an unsteady CFD analysis was conducted using the developed UDF as a proof of concept study for further research.

1. INTRODUCTION

With the steady growth of air traffic around the world it is anticipated that passenger demand will double in the next 20 years [1]. Therefore, in order to carry on with the goals set by the European Commission for 2020 and beyond [2] there is a need for more aerodynamically efficient aircraft.

Fixed (rigid) wing aircraft are normally optimised for a particular design point in each phase of flight and hence, optimised for a fixed set of parameters (e.g. altitude,

Mach number, weight). However, during real flight, these parameters can change, which means that the aircraft actually operates in sub-optimal conditions. Furthermore, the presence of discrete surfaces (e.g. ailerons, and high-lift devices) will create instabilities in the flow, which contribute to drag and noise [3] making the aircraft less fuel efficient.

The aforementioned issues of fixed wings can be improved using adaptable or morphing wings, which can be continuously deflected in-flight to produce optimal performance throughout the entire flight envelope. This can also contribute to the increase of lift and reduction of aerodynamic noise (by filling the gaps formed by discrete surfaces [4]).

Overall, the following advantages that are expected from morphing wings include:

- Higher aerodynamic efficiency due to the optimised lift-to-drag ratio, which would lead to an extended cruise range [5], [6]. For instance, Fig. 1 shows the variable camber effect on the L/D ratio [7].
- Reduction in aerodynamic noise [4].
- More operational flexibility with mission adaptability.

Nevertheless, the morphing wings may add some complexities to the design and analysis process as follows:

- New adaptive materials need to be integrated for morphing application.

- Advanced control and optimization algorithms should be developed to provide the most advantageous improvements from a morphing configuration.
- And most importantly, accurate predictions of the forces (lift, drag) and moments acting on these morphing wings are needed in order to estimate the possible gains from such concept and whether or not these aerodynamic improvements outweigh the added weight and complexity of morphing wing systems.

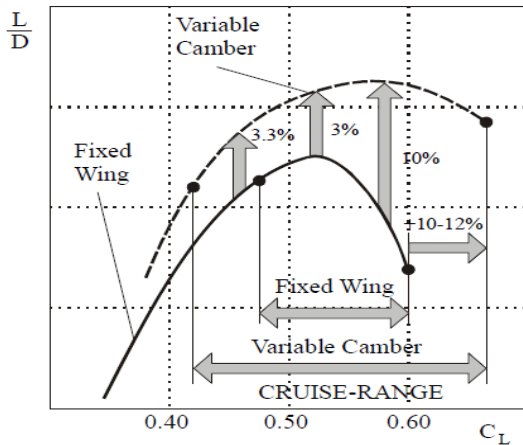


Figure 1. Variable camber effect on L/D ratio [7].

The aerodynamic modelling of morphing wings brings additional challenges to the field from a numerical point of view:

- Unique challenges presented by the large and rapid deformation of a wing moving at high speeds.
- Higher degrees of freedom that strongly influence the aerodynamics.
- The need for unsteady parametrization of geometry deformation to capture the deforming effects correctly.
- Efficient dynamic meshing methods that suit the deformation are needed.
- Appropriate turbulence modelling in order to capture the underlying physics of the problem.

To model a morphing airfoil with a deflecting trailing edge, we need a mathematical model to parametrize the geometry and its deformations as well as a dynamic meshing tool that allows for mesh 'movement' with the geometry. Finally, the numerical findings must be validated against other numerical or test results.

2. METHODOLOGY

Various numerical methods were used in order to analyse morphing wings. Steady and unsteady vortex-lattice methods (VLM) were more popular for morphing configurations, but they tend to have a limited accuracy with the unsteady version performing well with fast

morphing. VLM has previously been used to model an aircraft with morphing wings [8], to predict and optimise the lift-to-drag ratio of a variable camber morphing wing [6], and to compare the performance of an optimised camber and span morphing wings [9]. A doublet-lattice method (DLM) corrected by high accuracy CFD data was also used to model a wing tip morphing [10].

Most of recent aerodynamic optimization problems have typically used an aerodynamic model based on the Reynolds Averaged Navier Stokes (RANS) equations coupled with turbulence models. For instance, this technique has been applied to model both a morphing trailing edge and a full morphing wing [11], where it was found that a drag reduction of 1-5% was possible, depending on flight phase and conditions.

An alternative approach was explored in the literature where simulations of varying fidelity (e.g. VLM, Euler CFD, and RANS) were applied to study a span wise morphing wing [13]. However, most of the studies had to balance between accuracy and computational cost. That is why steady, reduced-order methods were widely applied in the analysis of morphing wings.

In order to overcome the inherent deficiency in this type of analysis, a methodology to parametrize an airfoil with a morphing trailing edge using a modified class shape transformation (CST) technique and a modified method for the parametrization of a fish bone active camber (FishBAC) concept are proposed [14]. These unsteady parametrization techniques are subsequently implemented in a user-defined function (UDF) which will be used to perform dynamic meshing in the commercial solver ANSYS Fluent.

3. UNSTEADY PARAMETERIZATION

In order to represent the morphing geometry of an airfoil, a parameterization method is required that has: 1) the flexibility to characterize a large set of airfoils, 2) sufficient robustness to yield a high fidelity, and 3) a smooth representation with a small set of control variables which gives adequate flexibility to deform the airfoil.

Reference [15] provided a comprehensive survey of parametric models, which are generally divided into eight categories: basis vector, domain element, partial differential equation (PDE), CAD-based, discrete approach, polynomial and spline, analytical and geometric, and freeform deformation (FFD).

A modified version of the polynomial based method CST (as originally presented by Kulfan [16]) was chosen for this work, due to reason (s) explained below.

3.1 CST Method

The CST method was chosen for this work for the following reasons:

- The easy and intuitive mathematical formulation.
- The possibility to represent any smooth airfoil in addition to other aerospace related shapes such as fuselage or nacelles.
- The smooth curves can be produced with a high level of accuracy and with no discontinuities.
- Easily extendable to 3D.
- Local control on different portions of the airfoil.
- Suitable for implementation in a UDF in ANSYS Fluent.

Eqs. 1-2 show the general mathematical formulation of the CST.

$$\zeta_u(\psi) = C_{N2}^{N1}(\psi)S_u(\psi) + \psi\Delta\zeta_u \quad (1)$$

$$\zeta_l(\psi) = C_{N2}^{N1}(\psi)S_l(\psi) + \psi\Delta\zeta_l \quad (2)$$

where:

$\psi = \frac{x}{c}$ and $\zeta = \frac{z}{c}$ are the non-dimensionalized coordinates with respect to the airfoil chord c . $C_{N2}^{N1}(\psi)$ is the class function. $S_u(\psi)$ and $S_l(\psi)$ are the upper and lower shape functions, respectively. $\Delta\zeta_u$ and $\Delta\zeta_l$ define, respectively, the upper and lower trailing edge thicknesses.

The general class function is defined in Eq. 3:

$$C_{N2}^{N1}(\psi) = \psi^{N1}(1-\psi)^{N2} \quad (3)$$

For a NACA type airfoil with a round nose and a pointed aft end (Fig. 2), the $C_{1.0}^{0.5}(\psi)$ class function is used, which forms the basis of the CST airfoil representation. Therefore, all the other airfoils are derived from the class function presented in Eq. 3.

The shape function, as defined in Eq.4, is composed of weighted Bernstein polynomials which are given in Eq. 5.

$$S(\psi) = \sum_{i=0}^p \overline{P(i)} B_{i,p}(\psi) \quad (4)$$

$$B_{i,p}(\psi) = \binom{p}{i} \psi^i (1-\psi)^{p-i} \quad (5)$$

where p is the order of the polynomial.

Each of these polynomials has a global effect on the airfoil shape, but the influence of each term decays relatively quickly. For instance, the effect of the 0th order shape function term declines quickly and its effect on the aft part of the airfoil is relatively small. To ensure that the deformation in the aft part will not have any effects on other non-deformed parts of the airfoil, it was ensured through numerical implementation that the rest of the airfoil remains static.

A supplementary leading edge shaping term was

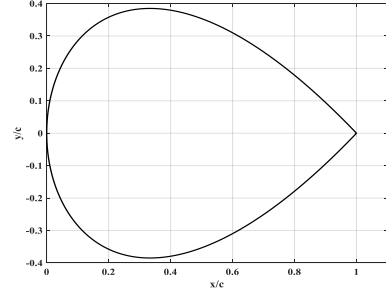


Figure 2. Unit Airfoil $C_{1.0}^{0.5}(\psi)$.

introduced to the representation by Kulfan [16] to increase the degree of control over the leading edge shape. The shaping term is formulated in Eq. 6.

$$x\sqrt{(1-x)}P_{LE}(1-x)^p \quad (6)$$

By adding the definitions of all the terms into Eqs. 1-2, these can be re-written as Eqs. 7-8.

$$\zeta_u(\psi) = \psi^{0.5}(1-\psi) \left[\sum_{i=0}^{pu} \overline{P_u(i)} \binom{p}{i} \psi^i (1-\psi)^{p_u-i} \right] + \psi\Delta\zeta_u + x\sqrt{(1-x)}P_{LE,u}(1-x)^{pu} \quad (7)$$

$$\zeta_l(\psi) = \psi^{0.5}(1-\psi) \left[\sum_{i=0}^{pl} \overline{P_l(i)} \binom{p}{i} \psi^i (1-\psi)^{p_l-i} \right] + \psi\Delta\zeta_l + x\sqrt{(1-x)}P_{LE,l}(1-x)^{pl} \quad (8)$$

Eqs. 7-8 fully describe any smooth airfoil given the CST coefficient of the targeted airfoil. The weighting coefficients are usually obtained by various fitting methods such as the least square method. All the qualities described make the CST method a suitable choice for several tasks requiring a smooth, flexible parametrization with a small set of design variables, particularly optimisation tasks.

The CST method was applied for wing optimisation studies in [17] that shows the use of CST in an inverse design process of airfoils with the emphasis on the

applicability of this method to various classes of geometry. In addition, it was applied for morphing wing optimization tasks in [18] where a 3D version of CST was successfully incorporated in an optimisation framework for morphing wings. Here, the researchers used a least square fit to match pre-existing CAD models and extract the CST coefficients that were used afterwards as optimisation variables.

3.2 Modified CST Method

Although the CST method has several characteristics that made it suitable for present application of the unsteady parametrisation of a morphing airfoil, it was necessary to modify it in order to parametrize a variable camber or variable thickness airfoil.

A time-dependant function was added to the classical formulation of the CST's representation of the upper and lower airfoil surfaces (i.e. Eqs. 7-8) to model variable camber. This resulted in a trailing edge deflection.

One of the properties of the CST method is that the higher the order of the term, the closer to the $\psi = 1$ point, therefore for a smooth trailing edge deflection the control term should be of a higher order than the Bernstein's polynomials order. A time dependant coefficient would control the speed, amplitude and frequency of the deflection. The general form of the term is presented in Eq. 9.

$$\zeta_{morph}(\psi, t) = y(t)\psi^{kp} \quad (9)$$

where:

$\zeta_{morph}(\psi, t)$ is the function which introduces the time dependency to CST method, $y(t)$ is a time dependant function to control the deflection rate and direction, while k is a coefficient that ensures a higher order than Bernstein's polynomials is achieved to limit the deformation closer to the trailing edge.

For instance, given that $y(t) = -0.05t$, then using a fifth order Bernstein polynomial for both upper and lower surfaces with $k = 3$, a zero trailing edge thickness introducing all the terms to Eqs. 7-8 will give us Eqs. 10-11.

$$\zeta_u(\psi) = \psi^{0.5}(1-\psi) \left[\sum_{i=0}^5 \overline{P_u(i)} \binom{5}{i} \psi^i (1-\psi)^{5-i} \right] + \quad (9)$$

$$x \sqrt{(1-x)} P_{LE,u} (1-x)^5 - 0.05t\psi^{15}$$

$$\zeta_l(\psi) = \psi^{0.5}(1-\psi) \left[\sum_{i=0}^5 \overline{P_l(i)} \binom{5}{i} \psi^i (1-\psi)^{5-i} \right] + \quad (10)$$

$$x \sqrt{(1-x)} P_{LE,l} (1-x)^5 - 0.05t\psi^{15} + 0.05t\psi^{15}$$

Fig. 3 shows the result of implementing Eqs. 10-11 at a time of 10s to obtain the desired trailing edge deflection. The modified method mentioned above acts directly on the surfaces of the airfoil. Another method to represent the airfoil is as the sum of thickness and camber part, for which the upper surface will be represented as a sum of the half-thickness and half camber distribution, and the lower surface is the subtraction of camber and thickness. Eqs. 12-13 define respectively the half thickness and half camber using CST method.

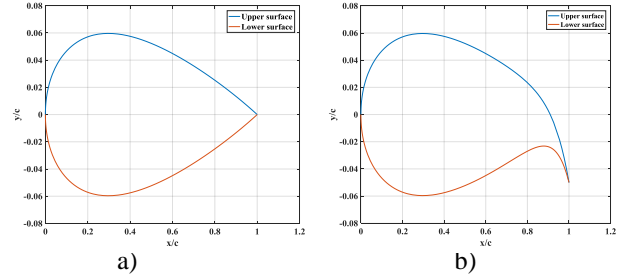


Figure 3. CST representation of NACA 0012.
a) at $t = 0s$, b) at $t = 10s$.

$$\zeta_t(\psi) = \psi^{0.5}(1-\psi) 0.5 \left[\sum_{i=0}^p \overline{(P_u(i) - P_l(i))} \binom{p}{i} \psi^i (1-\psi)^{p-i} \right] + \quad (11)$$

$$0.5\psi(\Delta\zeta_u - \Delta\zeta_l) + 0.5x\sqrt{(1-x)}(P_{LE,u} - P_{LE,l})(1-x)^p$$

$$\zeta_c(\psi) = \psi^{0.5}(1-\psi) 0.5 \left[\sum_{i=0}^p \overline{(P_u(i) + P_l(i))} \binom{p}{i} \psi^i (1-\psi)^{p-i} \right] + \quad (12)$$

$$0.5\psi(\Delta\zeta_u + \Delta\zeta_l) + 0.5x\sqrt{(1-x)}(P_{LE,u} + P_{LE,l})(1-x)^p$$

The upper and lower surface coordinates equation can be written as in Eqs. 14-15.

$$\zeta_u(\psi) = \zeta_t(\psi) + \zeta_c(\psi) \quad (13)$$

$$\zeta_l(\psi) = \zeta_t(\psi) - \zeta_c(\psi) \quad (14)$$

Using this formulation, we can separately act on specific parts of the airfoil while fixing the other parts. Fig. 4 shows a deformed NACA 0012 for two situations: a) the thickness was fixed while camber was changed, and b) the thickness was changed with fixed camber.

3.3 Techniques Inspired From Experiments

Several previous studies which combined an experimental and numerical investigation had to parametrize the prototype's deformation in a 'steady' fashion to produce comparative results for validations.

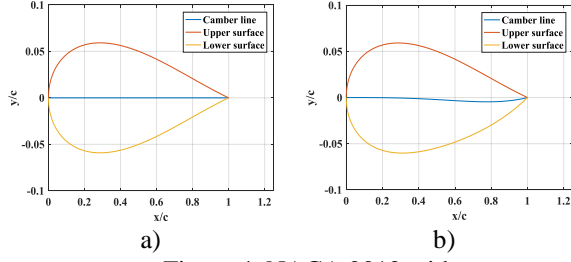


Figure 4. NACA 0012 with

- a) Fixed thickness and variable camber at $t = 10s$.
b) Fixed camber and variable thickness at $t = 10s$.

Therefore, it is essential to reproduce the parametrization process but with the addition of the unsteady effects that will give the ability to compare morphing CFD results with those available in literature.

One of the experiments of interest is the FishBAC parametrization. Reference [19] used a relatively simple approach to model a NACA 0012, which undergoes trailing edge deflections starting from different chord stations and for various maximum deflections. The baseline is morphed by adding camber to a specified region of the chord.

Their model is constructed using various parameters; the start of morphing is given by the parameter x_{te} , and the airfoil shape is built up by the accumulation of the NACA 0012 thickness distribution and a parametrically defined camber line.

The NACA four series thickness distribution is defined in Eq. 16 [20] :

$$y_t = (th/c) \begin{pmatrix} 0.2969\sqrt{x} - 0.1260x - 0.3516x^2 \\ +0.2843x^3 - 0.1015x^4 \end{pmatrix} \quad (15)$$

where y_t is the thickness distribution, x is the non-dimensional chord, th is the non-dimensional airfoil thickness ($th = 0.12$ for a NACA 0012).

A third order polynomial (Eq. 17) was used to define the camberline of the morphing part of the airfoil, and was parametrized to have a direct control over the amount of trailing edge maximum deflection:

$$y_c = \begin{cases} 0, & 0 \leq x < x_s \\ -w_{te} \cdot (x - x_s)^3 / (1 - x_s)^3, & x \geq 0 \end{cases} \quad (16)$$

where the w_{te} is the value of maximum deflection at the trailing edge, the thickness is then added to the camber distribution at right angles and the upper and lower coordinates of the surface could be represented as such.

This simple parametrization could be extended to add a time dependency, for instance it is possible to introduce a periodic motion as in Eq. 17:

$$y_c = \begin{cases} 0, & 0 \leq x < x_s \\ -w_{te} \sin(\pi t / T) (x - x_s)^3 / (1 - x_s)^3, & x \geq 0 \end{cases} \quad (17)$$

where t is time and T is the period of the motion. It is possible to numerically impose a criterion so that the deformation would stop once it reaches the desired maximum deflection.

4. DYNAMIC MESHING

Many physical problems in fluid dynamics involve moving boundaries such as flutter behaviour, blood flow through veins, flapping wings etc. In order to get efficient and accurate solution of the unsteady flow computation, reliable methods for moving the computational grid are necessary, especially that regenerating the mesh would be time consuming and computationally expensive. Some available commercial software offer some capabilities for dynamic meshing such as ANSYS Fluent.

ANSYS Fluent is a finite volume based solver where the domain is discretised into a finite set of control volumes and the general conservation equations for mass, momentum, energy, species, etc. are solved on this set of control volumes. The package provides a comprehensive modelling capability for a wide range of incompressible and compressible, laminar and turbulent fluid flow problems for both steady and transient analysis [21].

Dynamic meshing is controlled by the bias of secondary development of a UDF, which controls macros and defines the required deformation. The DEFINE_GRID_MOTION macro [21] was used to control each boundary node separately which made the relative motions between nodes possible. Consequently, this allowed modelling of deforming non-rigid bodies.

We implemented our modified parametrization techniques in UDF to enable the use the dynamic meshing capabilities available in ANSYS Fluent for flow analysis.

To update the mesh volume in the deformed regions, Fluent has three groups of mesh motion methods:

- Smoothing Methods.
- Dynamic Layering.
- Remeshing Methods.

For deformation problems such as morphing wings, the smoothing and remeshing method are of interest, however the remeshing technique is only available for tetrahedral mesh cells and our mesh is a quad dominant mesh, therefore we used the smoothing method.

Smoothing enables the mesh adjustment in the zones with the deformation. It permits the interior nodes to absorb the deformation without any change in the number of nodes or their connectivity. Two methods can be used for smoothing:

- *Spring-based*: where the edges between any two nodes are idealized as a network of springs.
- *Diffusion-based Smoothing*: where the diffusion equation governs the mesh motion.

Diffusion-based smoothing is generally more expensive computationally but tends to generate a better quality mesh, it allows preserving the mesh around the deforming body and making the far field absorb the deformation. For this reason, we performed our tests using this method, with a boundary distance diffusion function and a diffusion parameter ranging from 1 to 1.5 [21].

4.1 Deformed Mesh Quality

A set of meshes were generated using both Pointwise and ICEM mesh generators around a sharp trailing edge NACA 0012 airfoil. In addition, a mesh provided by NASA for validation purpose was tested for a morphing airfoil.

It was found that the C-type mesh has a low orthogonal quality under the recommended values by Fluent due to the presence of the wake-line (minimal orthogonal quality of 0.01). Tab. 1 shows the mesh quality evolution for a C-Type mesh.

A set of O-Grid meshes were tested, and the results of key mesh quality parameters are shown in Tab. 2.

Tab. 2 shows that unlike the C-type mesh, the O-type keeps an orthogonal quality above 0.01 which is required by the solver as a minimum criterion.

A mesh validation study was performed to see if it yields results close to other established solvers and experiments. NASA provides data for validation purposes for NACA 0012 [22], where the Reynolds number was 6 million and the Mach number was 0.15.

The software Pointwise was used for the mesh creation where the first cell height was chosen to get a dimensionless wall distance of $y^+ = 1$. In practice, the actual y^+ value was less than 1 in most of the simulations performed with a mesh size of 86,000 cells which is more than suitable for the models and cases simulated.

The two-equation $k-\omega$ SST turbulence model [23] was used for this case, along with the pressure velocity coupled solver and a coupled discretization method with second order spatial discretization for the gradients.

Fig. 5 and Fig. 6 show the lift and drag coefficients

Table 1. Evolution of various quality indicators depending on the deflection intensity for a NASA C-type mesh.

w_{te}	Minimum Orthogonal Quality	Maximum Ortho Skew	Maximum Aspect Ratio
0	1.17E-01	8.83E-01	2.99E+07
0.05	1.80E-03	9.98E-01	2.99E+07
0.1	9.03E-04	9.99E-01	2.99E+07
0.15	6.029E-04	9.993E-01	2.99E+07

obtained from Fluent compared with experimental data from [24]. Results obtained from Fluent gave good agreement with the CFL3D results provided by NASA [22] for the three angles of attack of 0° , 5° and 15° for both lift and drag coefficients. The experimental results agree well with Fluent results until $AoA = 15^\circ$ where the discrepancy is higher for drag coefficient. This is presumably due to the turbulence model used which tends to over-produce the turbulent kinetic energy; this makes the flow separation smaller than predicted.

Table 2. Evolution of various quality indicators depending on the deflection intensity for an O-type mesh.

w_{te}	Minimum Orthogonal Quality	Maximum Ortho Skew	Maximum Aspect Ratio
0	6.91E-01	3.09E-01	1.23E+04
0.05	1.94E-01	8.06E-01	1.23E+04
0.1	8.12E-02	9.19E-01	1.23E+04
0.15	4.43E-02	9.56E-01	1.23E+04

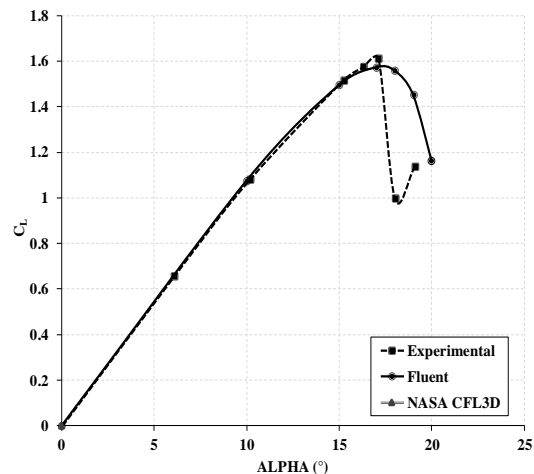


Figure 5. Lift coefficient plotted versus the angle of attack from Fluent results, Ladson experimental data [24] and NASA code CFL3D [22].

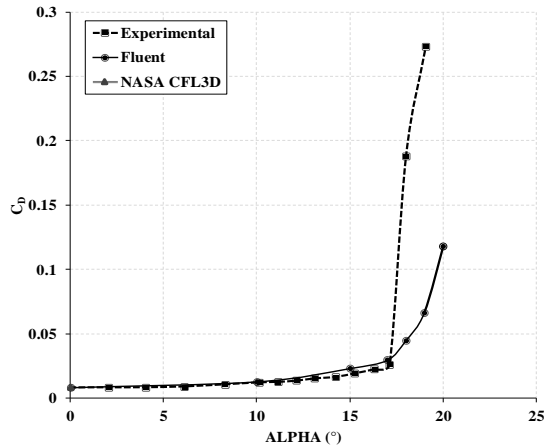


Figure 6. Drag coefficient plotted versus the angle of attack from Fluent results, Ladson experimental data [24] and NASA code CFL3D [22].

5. STEADY ANALYSIS OF MORPHING AIRFOIL

In order to study the effect of the mesh quality after deformation, a comparative study was conducted, where the FishBAC [19] morphing concept was represented by the modified parametrization method to assess the impact of the mesh deformation. The airfoil was deflected with a deflection value of $w_{te} = 0.05$ or 5% of the chord and a steady case simulation was performed at this deflection for the following two cases:

- *Deformed case*: the airfoil was deformed using the developed UDF to get into the final position where the deflection value is 0.05 then a steady simulation was run with this mesh.
- *Re-meshed case*: which consists of a re-generated mesh around the deflected airfoil.

Table 3. Parameters used for the CFD analysis.

Parameters	Value
Reynolds number	6.75×10^5
Chord	0.3m
Maximum deflection : w_{te}	0.05
Morphing start : x_s	75% of the chord
Angle of attack	0 to 10°

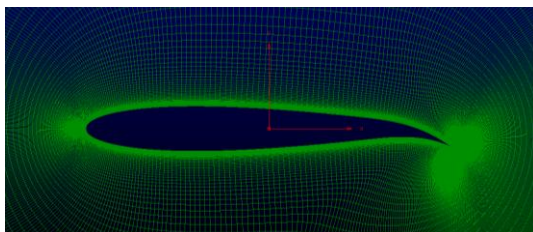


Figure 7. Mesh regenerated for the morphed NACA 0012 study.

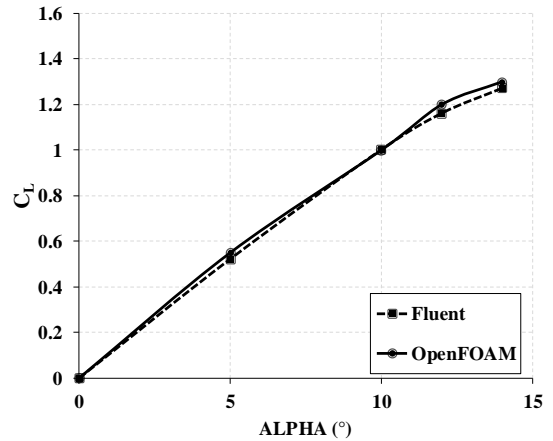


Figure 8. Lift coefficient for the baseline configuration NACA 0012.

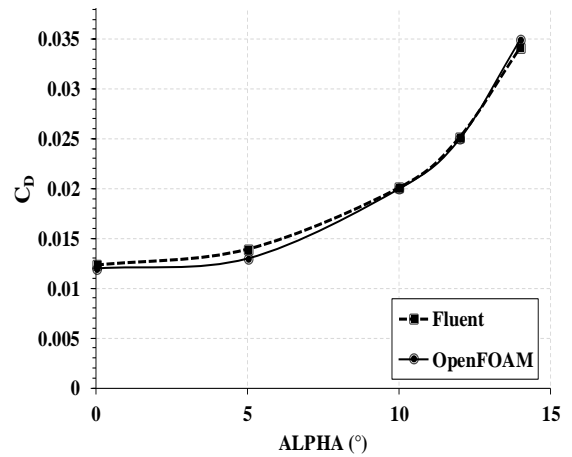


Figure 9. Drag coefficient for the baseline configuration NACA 0012.

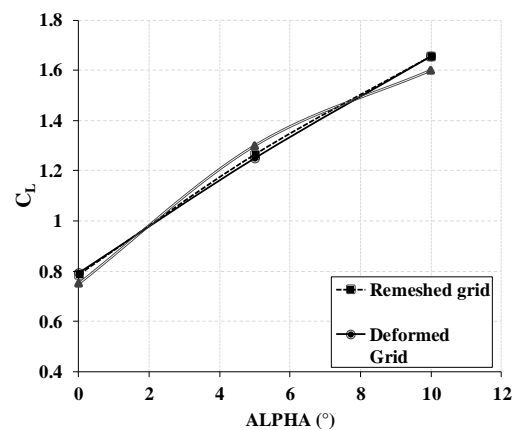


Figure 10. Lift coefficient comparison between a deformed mesh, re-meshed grid and results from OpenFOAM [19].

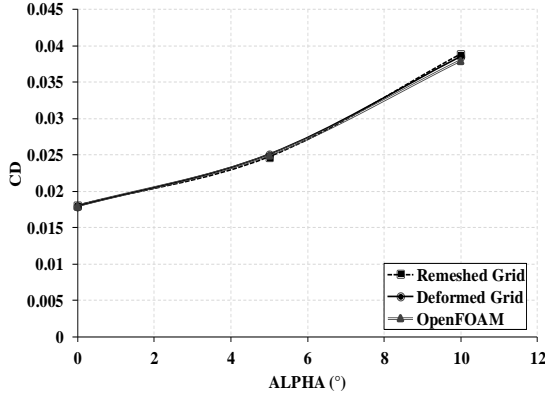


Figure 11. Drag coefficient comparison between a deformed mesh, re-meshed and results OpenFOAM [19].

The above cases were compared with the same simulation in [19], for which the flow conditions are listed in Tab. 3.

For the simulations, the same $k-\omega$ SST turbulence model is used in OpenFOAM analysis, a 2nd order discretization for the gradient, a coupled pressure-velocity scheme, and a flow Courant number of 1.

A pressure far field boundary condition was imposed on a domain which was scaled down by a factor of 0.3 in order to get the desired chord length and Reynolds number, making the far field about 30m away from the airfoil. Fig. 7 shows the computational grid around the morphed airfoil. All simulations were run until the lift and drag coefficients were flat, and continuity residuals dropped below 1×10^{-6} . Before studying the morphed configuration, the baseline NACA 0012 was analysed and the results compared with the ones obtained from OpenFOAM. The comparison shows very close results as demonstrated in Fig. 8 and Fig. 9.

Afterwards, a set of simulations was conducted in order to compare the deformed mesh, the re-meshed grid, and the results obtained from OpenFOAM for steady state simulations. Fig. 10 and Fig. 11 show the results obtained from the comparative study.

5.1 Morphed and Flapped NACA 0012 Study

In order to determine the effect of having a morphing airfoil, a comparative CFD analysis was conducted where a NACA 0012 was modified and a simple flap was added at the chord station 0.75c; the same morphing start location of the morphed airfoil. The flap was selected to have a maximum deflection value of 0.05 similar to the morphed case. Fig. 12 illustrates the two cases studied. The same flow conditions were applied to the flapped

airfoil. A structured mesh of 89,000 cells was generated with a value of $y^+ = 1$. Fig. 13 shows the computational grid used for this study.

6. RESULTS AND DISCUSSION

From the study performed on the deformed and re-generated mesh, we can observe that both the deformed and re-meshed grids gave very good agreement in the range of angle of attack studied. The discrepancy between the two cases was generally around or less than 1% as illustrated by Figs. 10 and Fig. 11. This clearly demonstrates that the mesh preserves a good quality after

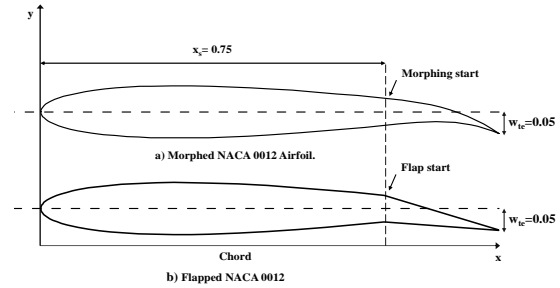


Figure 12. Two configurations investigated.

the deformation.

Fig. 14 to Fig. 16 show the results of lift coefficient, drag coefficient and aerodynamic efficiency (C_L/C_D) of the morphing and flapped airfoils, together with the baseline NACA 0012 results. Interesting trends appear in the data; first, we notice that for the same deflection angle, the morphing airfoil produces higher lift with an average increase in lift of about 17% compared with the flapped airfoil. This increase is accompanied with an average increase in drag of 14%.

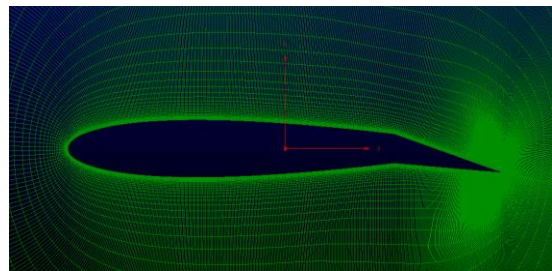


Figure 13. Mesh used for the flapped NACA 0012.

The aerodynamic efficiency graph (see Fig. 16) illustrates a trend where the morphed airfoil is aerodynamically more efficient (higher C_L/C_D ratio) in the majority of the angles of attack studied, with an average of 3% more aerodynamic efficiency for the morphing airfoil even though the flapped airfoil studied

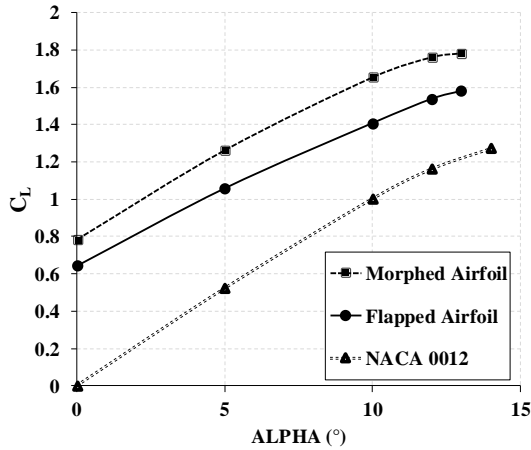


Figure 14. Lift coefficient comparison between original, morphed and flapped NACA 0012 airfoils.

had no gap between the main airfoil and the flap (which tends to cause extra drag).

7. UNSTEADY ANALYSIS OF MORPHING AIRFOIL

Using the developed UDF, unsteady analysis of the morphing airfoil was conducted at AoA = 10°, where the airfoil was morphed from the baseline NACA 0012 to a maximum trailing edge deflection of $w_{te} = 0.05$ over a time period of 6.75 sec. Fig. 17 and Fig. 18 show various flow field properties at different time steps where the unsteady trailing edge deflection is illustrated. More quantitative investigations will be conducted in the next stage of the research.

8. CONCLUSION

A study of morphing airfoil using a modified CST method and a user defined function was presented. The results for the deformed mesh were compared with a re-generated mesh to assess the accuracy of the dynamic

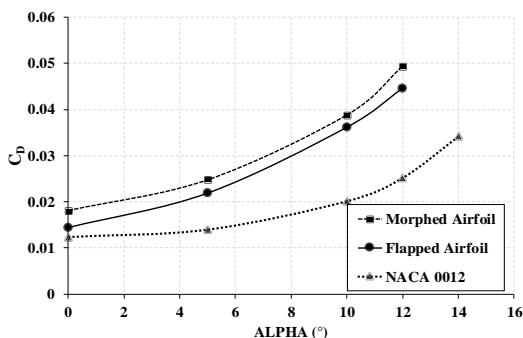


Figure 15. Drag coefficient comparison between original, morphed and flapped NACA 0012 airfoils.

meshing schemes. In addition, a comparative study between a morphed and flapped airfoil was presented

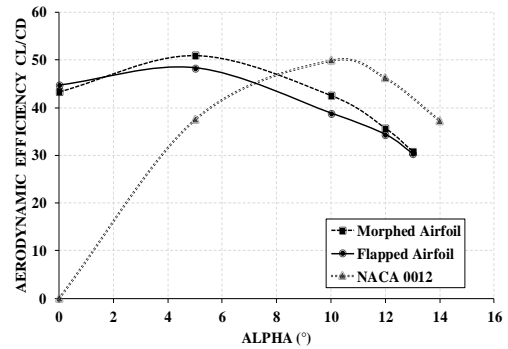


Figure 16. Aerodynamic efficiency vs angle of attack for original, morphed and flapped NACA 0012 airfoils.

alongside some preliminary results of the unsteady morphing airfoil investigation. The following conclusions can be made:

- The deformed mesh gave results comparable to a re-generated mesh with a discrepancy of approximately 1%.
- The morphing airfoil produced higher lift for the same deflection in comparison to a flapped airfoil, with an average increase in aerodynamic efficiency of 3%.

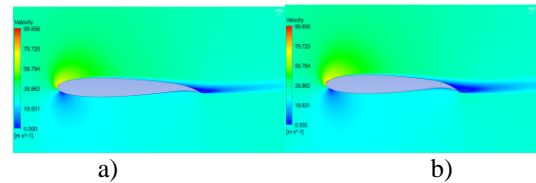


Figure 17. Velocity field for a morphing NACA 0012. a) at $t = 3s$, b) at $t = 6.75s$.

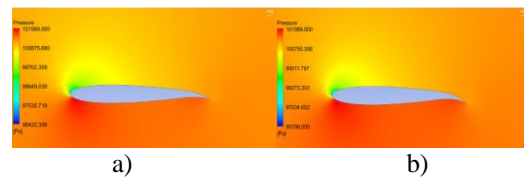


Figure 18. Pressure field for a morphing NACA 0012. a) at $t = 3s$, b) at $t = 6.75s$.

Future work will focus on the unsteady analysis of morphing airfoils and the quantifications of the differences found in various flow field properties between the steady and unsteady case, in addition to an extension to 3D morphing wing analysis.

ACKNOWLEDGEMENTS

The first author gratefully acknowledges the studentship funding received from the Engineering Modelling and

REFERENCES

- [1] Flightpath, A.C.A.R.E., (2011). 2050-Europe's Vision for Aviation. *Advisory Council for Aeronautics Research in Europe*. <http://www.acare4europe.com>.
- [2] Quentin, F. and Szodruch, J., (2010). Aeronautics and air transport: beyond vision 2020 (towards 2050). *Report for ACARE*. <http://www.acare4europe.com>.
- [3] Macaraeg, M., (1998). Fundamental investigations of airframe noise. In *4th AIAA/CEAS Aeroacoustics Conference* AIAA-98-2224.
- [4] Woods, B.K., Parsons, L., Coles, A.B., Fincham, J.H. and Friswell, M.I., (2016). Morphing elastically lofted transition for active camber control surfaces. *Aerospace Science and Technology*, 55, 439-448.
- [5] Szodruch, J. and Hilbig, R., (1988). Variable wing camber for transport aircraft. *Progress in Aerospace Sciences*, 25(3), 297-328.
- [6] Urnes, J. and Nguyen, N., (2013), A mission adaptive variable camber flap control system to optimize high lift and cruise lift to drag ratios of future n+ 3 transport aircraft. In *51st AIAA Aerospace Sciences Meeting including the New Horizons Forum and Aerospace Exposition* AIAA-2013-0214.
- [7] Monner, H.P., Breitbach, E., Bein, T. and Hanselka, H., (2000). Design aspects of the adaptive wing—the elastic trailing edge and the local spoiler bump. *The Aeronautical Journal*, 104(1032), 89-95.
- [8] Obradovic, B. & Subbarao, K., (2012). Modeling and Simulation of Morphing Wing Aircraft. *Morphing Aerospace Vehicles and Structures*, 48(2), 87–125.
- [9] Molinari, G. et al., (2011). Aero-Structural Optimization of Morphing Airfoils for Adaptive Wings. *Journal of Intelligent Material Systems and Structures*, 22(10), 1075–1089.
- [10] Cooper, J.E., Chekkal, I., Cheung, R.C.M., Wales, C., Allen, N.J., Lawson, S., Peace, A.J., Cook, R., Standen, P., Hancock, S.D. and Carossa, G.M., (2015). Design of a Morphing Wingtip. *Journal of Aircraft*, 52(5), 1394-1403.
- [11] Burdette, D.A., Kenway, G.K., Lyu, Z. and Martins, J., (2015). Aerostructural design optimization of an adaptive morphing trailing edge wing. In *56th AIAA/ASCE/AHS/ASC Structures, Structural Dynamics, and Materials Conference* AIAA-2015-1129.
- [12] Yang, Y., Ozgen, S., Yaman, Y., Ciarella, A., Hahn, M., Beaverstock, C. and Friswell, M.I., (2016). MDAO for Aerodynamic Assessment of a Morphed Wing for the Loiter Segment of a UAV Flight Mission. In *24th AIAA/AHS Adaptive Structures Conference* AIAA-2016-0314.
- [13] Beaverstock, C. S., Fincham, J., Friswell, M. I., Ajaj, R. M., De Breuker, R., & Werter, N. (2014). Effect of Symmetric & Asymmetric Span Morphing on Flight Dynamics. In *AIAA Atmospheric Flight Mechanics Conference*, AIAA SciTech Forum, AIAA 2014-0545. doi: 10.2514/6.2014-0545.
- [14] Woods, B.K., Bilgen, O. and Friswell, M.I., (2014). Wind tunnel testing of the fish bone active camber morphing concept. *Journal of Intelligent Material Systems and Structures*, 25(7), 772-785.
- [15] Samareh, J.A., (2001). Survey of shape parameterization techniques for high-fidelity multidisciplinary shape optimization. *AIAA Journal*, 39(5), 877-884.
- [16] Kulfan, B. and Bussolletti, J., (2006). "Fundamental" Parameteric Geometry Representations for Aircraft Component Shapes. In *11th AIAA/ISSMO multidisciplinary analysis and optimization conference* AIAA-2006-6948.
- [17] Lane, K. and Marshall, D., (2010). Inverse airfoil design utilizing CST parameterization. In *48th AIAA Aerospace Sciences Meeting Including the New Horizons Forum and Aerospace Exposition* AIAA-2010-1228.
- [18] De Gaspari, A. and Ricci, S., (2015). Knowledge-based shape optimization of morphing wing for more efficient aircraft. *International Journal of Aerospace Engineering*, vol. 2015, Article ID 325724, 19 pages, 2015. doi:10.1155/2015/325724
- [19] Woods, B.K., Fincham, J.H. and Friswell, M.I., (2014). Aerodynamic modelling of the fish bone active camber morphing concept. In *Proceedings of the RAeS Applied Aerodynamics Conference, Bristol, UK*.
- [20] Jacobs, E.N., Ward, K.E. and Pinkerton, R.M., (1935). The characteristics of 78 related airfoil sections from tests in the variable-density wind tunnel. NACA Report 460.
- [21] ANSYS® Fluent, 17.0, help system, ANSYS FLUENT Theory Guide, ANSYS, Inc.
- [22] Rumsey, C., Smith, B., & Huang, G. (2012). Langley research center turbulence modeling resource. <http://turbmodels.larc.nasa.gov>
- [23] Menter, F.R., (1994). Two-equation eddy-viscosity turbulence models for engineering applications. *AIAA Journal*, 32(8), 1598-1605.
- [24] Ladson, C.L., Hill, A.S. and Johnson Jr, W.G., (1987). Pressure distributions from high Reynolds number transonic tests of an NACA 0012 airfoil in the Langley 0.3-meter transonic cryogenic tunnel. NASA-TM-100526.